

# Robust Chemiresistive Behavior in Conductive Polymer/MOF Composites

Heejung Roh, Dong-Ha Kim, Yeongsu Cho, Young-Moo Jo, Jesús A. del Alamo, Heather J. Kulik,\* Mircea Dincă,\* and Aristide Gumyusenge\*

Metal-organic frameworks (MOFs) are promising materials for gas sensing but are often limited to single-use detection. A hybridization strategy is demonstrated synergistically deploying conductive MOFs (cMOFs) and conductive polymers (cPs) as two complementary mixed ionic-electronic conductors in high-performing stand-alone chemiresistors. This work presents significant improvement in i) sensor recovery kinetics, ii) cycling stability, and iii) dynamic range at room temperature. The effect of hybridization across well-studied cMOFs is demonstrated based on 2,3,6,7,10,11-hexahydroxytriphenylene (HHTP) and 2,3,6,7,10,11-hexaiminotriphenylene (HITP) ligands with varied metal nodes (Co, Cu, Ni). A comprehensive mechanistic study is conducted to relate energy band alignments at the heterojunctions between the MOFs and the polymer with sensing thermodynamics and binding kinetics. The findings reveal that hole enrichment of the cMOF component upon hybridization leads to selective enhancement in desorption kinetics, enabling significantly improved sensor recovery at room temperature, and thus long-term response retention. This mechanism is further supported by density functional theory calculations on sorbate–analyte interactions. It is also found that alloying cPs and cMOFs enables facile thin film co-processing and device integration, potentially unlocking the use of these hybrid conductors in diverse electronic applications.

their inherent porosity, high surface area, and high molecular adsorptivity.<sup>[1–5]</sup> Particularly for MOF-based sensing, the chemical versatility of metal nodes and organic ligands renders MOFs attractive for molecularly tuning both sensitivity and selectivity toward a wide range of analytes.<sup>[6,7]</sup> Pore size control also provides an additional knob for size-exclusion based sensing.<sup>[8–10]</sup> Electrically conductive MOFs (cMOFs) are of particular interest in chemiresistive sensors leveraging their conductance modulation within the framework upon host-guest interaction to identify and quantify the guest molecules.<sup>[11,12]</sup> However, deploying cMOFs in sensors still faces technological challenges: i) MOFs are commonly synthesized as powders and their integration into electronic devices is challenging. Typically, MOF powders are pressed into pellets or suspended as pastes to form active layers, leading to poor performance reproducibility and loss in inherent properties at the expense of additive loadings.<sup>[13–15]</sup> Layer-by-layer liquid epitaxy and surface-supported MOF growth, though yet to be demonstrated for a wide library of MOF structures, have emerged as promising alternative processing strategies for applications requiring high quality thin films.<sup>[16–18]</sup> ii) MOF-based chemical sensors are often dosimetric due to limited reversibility which hinders practical use.<sup>[19,20]</sup>

## 1. Introduction

Metal-organic frameworks (MOFs) are attractive for catalysis, energy storage, chemical capture, as well as sensing owing to

H. Roh, A. Gumyusenge  
 Massachusetts Institute of Technology  
 Department of Materials Science & Engineering  
 77 Massachusetts Ave, Cambridge, MA 02139, USA  
 E-mail: [aristide@mit.edu](mailto:aristide@mit.edu)

 The ORCID identification number(s) for the author(s) of this article can be found under <https://doi.org/10.1002/adma.202312382>

© 2024 The Authors. Advanced Materials published by Wiley-VCH GmbH. This is an open access article under the terms of the [Creative Commons Attribution-NonCommercial-NoDerivs](https://creativecommons.org/licenses/by/4.0/) License, which permits use and distribution in any medium, provided the original work is properly cited, the use is non-commercial and no modifications or adaptations are made.

DOI: 10.1002/adma.202312382

H. Roh, D.-H. Kim, Y. Cho, Y.-M. Jo, H. J. Kulik, M. Dincă  
 Massachusetts Institute of Technology  
 Department of Chemistry  
 77 Massachusetts Ave, Cambridge, MA 02139, USA  
 E-mail: [hjkulik@mit.edu](mailto:hjkulik@mit.edu); [mdinca@mit.edu](mailto:mdinca@mit.edu)

Y. Cho, H. J. Kulik  
 Massachusetts Institute of Technology  
 Department of Chemical Engineering  
 77 Massachusetts Ave, Cambridge, MA 02139, USA

J. A. del Alamo  
 Massachusetts Institute of Technology  
 Department of Electrical Engineering and Computer Science  
 77 Massachusetts Ave, Cambridge, MA 02139, USA

J. A. del Alamo  
 MIT-IBM Watson AI Lab  
 75 Binney St, Cambridge, MA 02139, USA

Particular to gas sensing, cMOF-based detection of gases typically involves a combination of physical adsorption and chemical interactions.<sup>[5]</sup> For instance, ligand designs to form electron rich coordination sites favorable for attracting ubiquitous polar gas molecules through Van der Waals interactions have been demonstrated.<sup>[5]</sup> In addition, transition-metal nodes in these cMOFs primarily drive the majority of chemiresistive sensing owing to strong Lewis acid-base reactions between the metal nodes and analytes, especially polar gas molecules.<sup>[19,21,22]</sup> Consequently, 2D-conjugated ligands, namely 2,3,6,7,10,11-hexahydroxytriphenylene (HHTP) and 2,3,6,7,10,11-hexaiminotriphenylene (HITP), in combination with common nodes (Cu, Ni, Co) have been widely studied in chemiresistive gas sensors owing to their excellent and tunable electrical conductivity (which enables detection based on resistance change), as well as their facile synthesizability.<sup>[18,23–25]</sup> In that regard, gases such as NH<sub>3</sub>, H<sub>2</sub>S, and other volatile organic compounds have been reliably detected using cMOF-based sensors.<sup>[24]</sup>

NO<sub>2</sub> is one of the commonly emitted toxic gases that remain challenging to detect, even using conductive MOFs, especially at room temperature. Though cMOFs have shown promising performance for NO<sub>2</sub> detection,<sup>[26]</sup> irreversible sensing remains a major challenge due to the formation of stable coordination complexes, a trait that enables high sensitivity. Reversible detection of NO<sub>2</sub> at room temperature using MOFs becomes an inherent challenge due to strong binding behaviors, arising from NO<sub>2</sub>'s tendency to extract electrons from metal nodes (e.g., Cu<sup>1+</sup>) and form coordination complexes (e.g., 1) N-nitro, 2) O-nitrito, or 3) O, O' bidentate)<sup>[27,28]</sup> following the reaction below.



Due to this charge transfer, the cMOF's electron density distribution is perturbed thus translating into detectable resistance changes. cMOF-based chemiresistors have thus been studied as a promising technology for NO<sub>2</sub> gas sensing.<sup>[24]</sup> To achieve sensor reversibility, approaches such as the use of elevated temperature, incorporation of noble metal catalysts, photoactivation utilizing specific wavelength, and incorporation of heavy-metal nanoparticles have been reported to improve recovery kinetics, which still hamper real-world deployments.<sup>[21,22,24,29]</sup> In fact, these approaches remain the state-of-the-art, despite unique and promising features of cMOFs for NO<sub>2</sub> detection.<sup>[24,30]</sup> For real-world use, these approaches remain too costly, challenging to generalize, and user-unfriendly, thus calling for innovative strategies to fully leverage the affinity of MOFs toward NO<sub>2</sub>.

Efforts to expand the library of MOFs used in sensing applications have led to the utilization of polymer/MOF hybrids when direct film growth of MOFs is challenging.<sup>[13–15]</sup> However, this approach often results in a compromise between processability and inherent properties. That is, MOFs are typically blended with polymer additives, which are often insulating polymers, thus masking the intrinsic properties of the MOF components.<sup>[13–15]</sup> Here we report a new concept to synergistically marry sensing performance and processability, especially for detecting NO<sub>2</sub> gas at room temperature. We form hybrid films using designer conjugated polymers (cPs) and conductive MOFs to improve: i) The

sensitivity compared to pristine cMOFs, stemming from the increased density of the active material in the sensor. ii) Chemical selectivity via the incorporation of systematically functionalized cPs with selective and labile binding with NO<sub>2</sub>. iii) Regeneration of active sites within the sensing material, and consequently, long-term reliability at room temperature, due to improved kinetics of molecular exchange and a thermodynamically enhanced desorption process. And last, iv) solution processability via facile deployment methods (e.g., spin-coating, blade-coating, screen-printing, etc.), which is not readily unattainable in pristine MOFs.

## 2. Results and Discussion

### 2.1. Designing Conductive Polymer/MOF Films for Chemiresistive Devices

To form the newly designed polymer/MOF composite, we use a semicrystalline, mixed ionic-electronic conductive polymer (cP) based on 3,4-propylenedioxythiophene (ProDOT) and 2,1,3-benzothiadiazole (BTD),<sup>[31]</sup> and form hybrid films with 2D cMOFs (Figure 1a–c; Figures S1 and S2, Supporting Information). We select the ProDOT-BTD cP for its reversible redox-activity, low onset oxidation voltage, charge capacity, electrical conductivity to enhance the device response in presence of the analyte.<sup>[32,33]</sup> Particularly, the cP is designed to serve as a secondary NO<sub>2</sub>-affine component endowed by its polar sidechains,<sup>[34–37]</sup> as well as a binding matrix to physically unify cMOF crystallites and improve electrical communication throughout the bulk (Figure 1c,d). We then select two classes of cMOFs based on HHTP and HITP ligands (Figure 1a), which typically exhibit irreversible gas sensing behaviors in their pristine form. As shown in Figure 1e and Figure S2, Supporting Information, the X-ray diffraction peaks corresponding to pristine cMOFs remain unchanged upon hybridization without peak shifts, indicating that the structure of the cMOF remains undisturbed and well-preserved. We then study diverse metal nodes, which have shown promising performance in chemiresistive devices via molecular interactions between analyte gases and coordination sites.<sup>[38]</sup> All six cMOF combinations, namely M<sub>3</sub>(ligand)<sub>2</sub>, where M is either Co, Ni, or Cu and the ligand HHTP (X = O) or HITP (X = NH), were first synthesized and respective structures were verified through powder X-ray diffraction (PXRD) analysis (Figure S2, Supporting Information).

Scanning electron microscope (SEM) images show that the hybrid cP@cMOFs films are homogeneous and cMOFs crystallites are uniformly embedded in the cP matrix (e.g., cP@Cu<sub>3</sub>HHTP<sub>2</sub>, Figure 1c). This is in contrast with pristine cMOF films which show micro-cracks and pristine cP with a smooth texture (Figure 1a,b). We also use atomic force microscopy imaging to compare the surface roughness of drop-casted films, revealing smoother surfaces in cP@cMOFs compared to pristine cMOFs with *R*<sub>q</sub> values of 97.5 and 195 nm, respectively, owing to the presence of the cP with *R*<sub>q</sub> value of 22.7 nm (Figure S3a–c, Supporting Information). Furthermore, as corroborated by surface analysis using X-ray photoelectron spectroscopy (XPS) and Raman spectroscopy (probing depths of 10 and 645 nm, respectively), the cP shows to constitute most of the outermost layer of the composite films (at least ≈10 nm), engulfing cMOFs

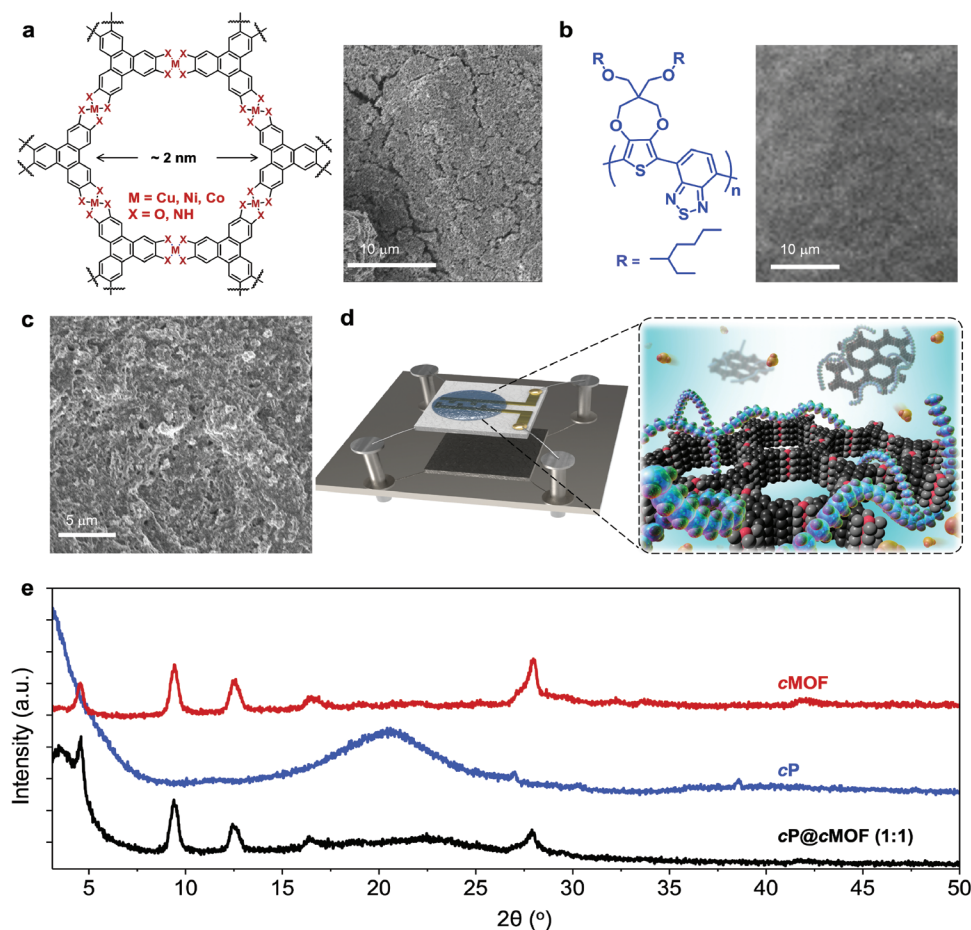


**Figure 1.** Hybridization between conductive polymers and MOFs for robust chemiresistors. a,b) Chemical structure and representative SEM images of 2D cMOFs,  $M_3(\text{ligand})_2$  (e.g.,  $(\text{Cu}_3\text{HHTP}_2)_2$ ) and cP. c) SEM image of cP@cMOFs (1:1, w/w). d) Schematic illustration of sensing device and interaction between cP@cMOF and gas analyte. e) PXRD spectra of 2D cMOF ( $\text{Cu}_3\text{HHTP}_2$ ), cP, and corresponding cP@cMOFs (1:1, w/w).

crystallites. At such shallow depths, the distinctive metal peaks from the cMOF component were absent in high-resolution XPS spectra of hybrid films (Figure S4, Supporting Information). At the same time, corresponding Raman spectra were identical to that of pristine cP (Figure S5, Supporting Information) indicative of a predominantly polymer-enriched interface in the hybrid films. We hypothesize that with this architecture, the semicrystalline and  $\text{NO}_2$ -affine polymer would also contribute to the adsorption of gas molecules into sensor's channel area and enhance the overall sensitivity of the sensors. That is, i) the conductive backbone is flanked with polar sidechains favoring the permeability of gas molecules into the active area across entire active channel,<sup>[29–32]</sup> and ii) cP serves as a conductive matrix binding MOF crystallites throughout the bulk thus promoting efficient charge transport upon resistance change. By interlinking the crystallites throughout the film bulk, the cP thus helps reduce inter-particles resistance, a dominant behavior in pristine MOFs, and enhances the performance of chemiresistors based on polymer/MOF composites (Figure 1c,d). The pasty nature of the solution processed cP was also envisioned to promote greater film integrity and hence device reliability and stability.

## 2.2. Gas Sensing Performance of cP@cMOFs

To test the effect of hybridization on gas sensing performance, we fabricated chemiresistive sensors using the cP@cMOFs combinations discussed above. Further details on the sensor fabrication steps and device dimensions are provided in the Experimental Section and illustrated in Figure S6, Supporting Information. As shown in Figure 2a, all sensors based on pristine cMOFs exhibited relatively low responses ( $R_{\text{air}}/R_{\text{gas}}$  or  $R_{\text{gas}}/R_{\text{air}} < \approx 2$ , where  $R_{\text{air}}$  and  $R_{\text{gas}}$  denote resistance in air and gas, respectively) as well as poor sensing reversibility. Upon hybridization with cP (e.g., 1:1 weight ratio between cP and cMOF), the sensing response, and most importantly, the sensing reversibility was significantly enhanced across all cMOFs (Figure 2a–c and Figure S7, Supporting Information). This performance enhancement was most exemplified in cP@ $\text{Ni}_3(\text{HITP})_2$  exhibiting a 23.9-fold improvement in sensor response relative to pristine  $\text{Ni}_3(\text{HITP})_2$  (Figure 2c). Note that, in its pristine form the cP yields sensors with undetectable response, and the same effect could not be induced when the hybridization is done with corresponding ligands (HHTP or HITP) instead of cMOFs, or other commonly studied conductive materials such as carbon nanotubes (CNTs) (Figures S8 and S9,

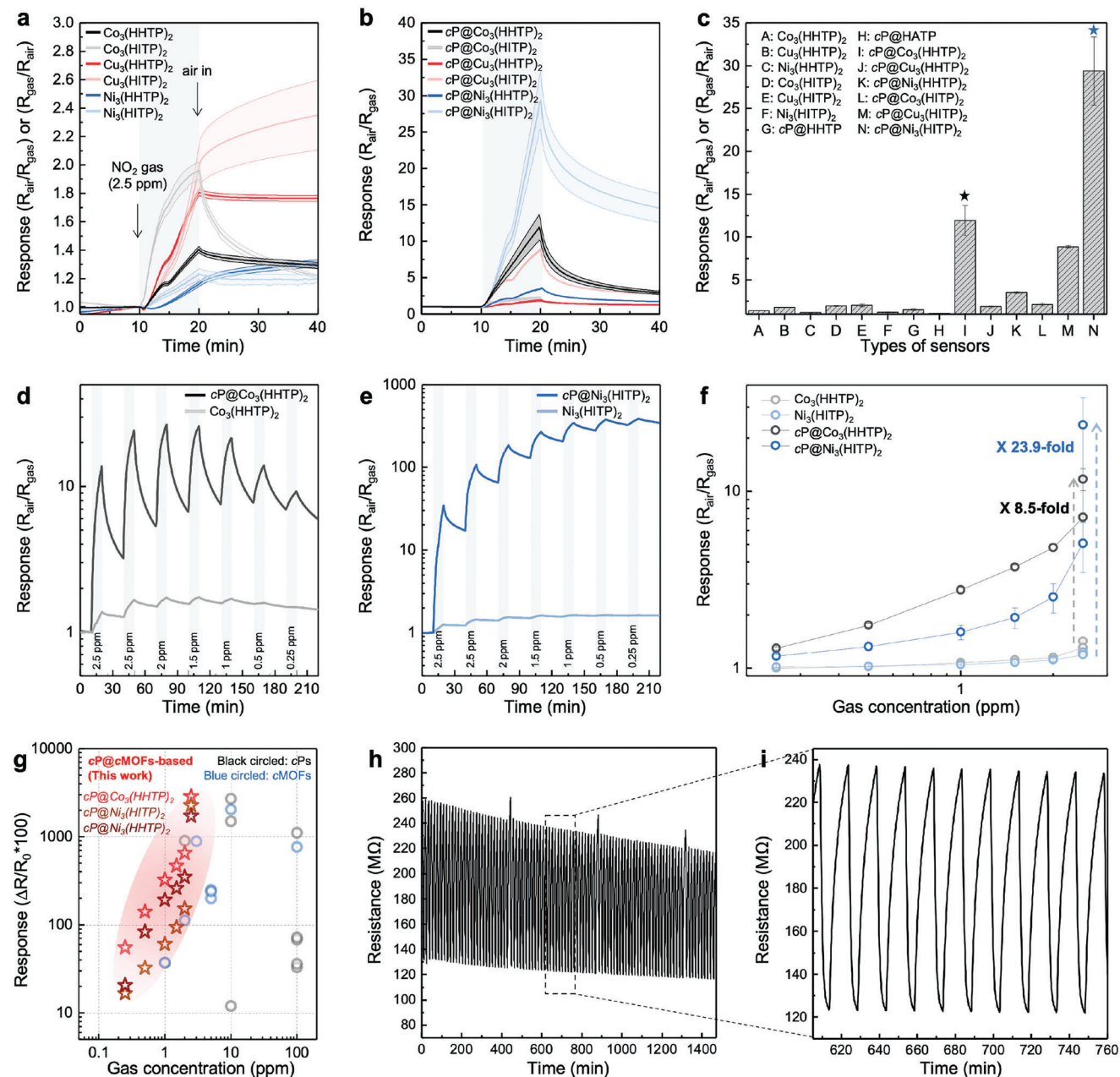


**Figure 2.** Sensing performance evaluation in  $cP@cMOF$ -based chemiresistors. Response graphs of a) 6 different pristine  $cMOFs$  and b)  $cP@cMOFs$  with 1:1 ratio. c) Response of all the sensors including pristine  $cMOFs$ ,  $cP@ligands$ , and  $cP@cMOFs$  ( $N \geq 3$ ). d) Response graphs of  $Co_3(HHTP)_2$  and  $cP@Co_3(HHTP)_2$  toward 2.5–0.25 ppm  $NO_2$  gas. e) Response graphs of  $Ni_3(HITP)_2$  and  $cP@Ni_3(HITP)_2$  toward 2.5–0.25 ppm  $NO_2$  gas. f) Response of  $Co_3(HHTP)_2$ ,  $Ni_3(HITP)_2$ ,  $cP@Co_3(HHTP)_2$ , and  $cP@Ni_3(HITP)_2$  toward 2.5–0.25 ppm  $NO_2$  gas ( $N \geq 3$ ). g) Responses of reported 2.5–0.25 ppm  $NO_2$  sensors using  $cP$  or  $cMOFs$ , operating at RT.<sup>[19,21,22,29,39–49]</sup> h) Operational stability of a  $cP@Co_3(HHTP)_2$  sensor under 97 cyclic exposures (1 ppm  $NO_2$ , 5 min exposure, 10 min air recovery), including i) an enlargement around  $t = 605$ –760 min.

Supporting Information). This behavior thus underscores the importance of utilizing a  $cP$  to hybridize with the porous  $cMOFs$  and synergistically enhance sensing response and reversibility.

Furthermore, the hybridization was beneficial to the sensitivity level of the sensor devices as illustrated in the dynamic resistance changes with  $NO_2$  concentrations down to 0.25 ppm (Figure 2d–f). In terms of sensitivity, we found that, upon optimization of the  $cP$  content in the hybrid films (Figures S10–S15, Supporting Information),  $cP@Ni_3(HITP)_2$  demon-

strated the most pronounced initial response in the presence of  $NO_2$ , albeit its relatively modest reversibility compared to the  $cP@Co_3(HHTP)_2$  analog. Also noteworthy, among all hybrid combinations,  $cP@Co_3(HHTP)_2$  exhibited the most dynamic resistive behavior and reversibility enhancement in comparison to its pristine counterpart. Nonetheless, across all six  $cMOFs$ , the hybridization was shown to enhance the sensing response compared to pristine constituents (Figure 2g) while conserving the selectivity level toward  $NO_2$  gas (Figures S16 and S17,

**Table 1.** Comparison of current results to state-of-the-art NO<sub>2</sub> sensing at room temperature using cP- and cMOFs-based chemiresistors.

Sensing material	Response [ $\Delta R/R_0 \times 100\%$ ]	Cyclability (# of cycles)	LOD [ppm]	Refs.
PPy thin film	12 @ 10 ppm	3	10	[39]
PT thin film	33 @ 100 ppm	3	10	[40]
PANI-nanofibers	1500 @ 10 ppm	n.r.	10	[41]
PANI thin film	1110 @ 100 ppm	n.r.	10	[42]
Ag-PPy	68 @ 100 ppm	n.r.	5	[43]
PANI fibers	900 @ 2 ppm	n.r.	1	[44]
ZnO/PANI nanoflake	2700 @ 10 ppm	n.r.	0.01	[45]
DBSA-doped PPy-WO <sub>3</sub>	72 @ 100 ppm	3	5	[46]
PPy/ $\alpha$ -Fe <sub>2</sub> O <sub>3</sub>	36 @ 100 ppm	3	10	[47]
PEI-doped PNDIT2/IM	37.2 @ 1 ppm	15	0.1	[48]
Cu <sub>3</sub> (HHTP) <sub>2</sub> /Fe <sub>2</sub> O <sub>3</sub> hybrids	≈200 @ 5 ppm	7	0.2	[21]
Pd@Cu <sub>3</sub> (HHTP) <sub>2</sub>	≈250 @ 5 ppm	14	1	[22]
Pt@Cu <sub>3</sub> (HHTP) <sub>2</sub>	≈240 @ 5 ppm	14	1	[19]
PtRu@Cu <sub>3</sub> (HHTP) <sub>2</sub>	112.8 @ 2 ppm	7	0.2	[19]
Pt@Cu <sub>3</sub> (HHTP) <sub>2</sub> thin film	890.1 @ 3 ppm	n.r.	0.1	[26]
Cu-Salphen-MOF	766 @ 100 ppm	5	1	[50]
Single crystal Ti-MOF (FIR-120)	2040 @ 10 ppm	5	1	[29]
CPs@CoHHTP 1:4	2863 @ 2.5 ppm	97	0.25	This work
CPs@NiHHTP 1:1	2282 @ 2.5 ppm	10	0.25	This work
CPs@NiHHTP 8:1	1716 @ 2.5 ppm	10	0.25	This work

Supporting Information), given uniform distribution of the components within the bulk (Figure S18, Supporting Information). Most importantly, all cP@cMOFs-based sensors demonstrated enhanced cycling reversibility compared to their pristine counterparts (Figure 2h,i; Figures S10 and S14, Supporting Information). Particularly, cP@Co<sub>3</sub>(HHTP)<sub>2</sub>-based sensors exhibit stable and reversible performance up to 97 cycles (Figure 2h,i). To the best of our knowledge, our work presents the highest number of cycling tests with stable reversibility among all cMOFs- or cP-based chemiresistive sensors reported to date (Table 1).<sup>[21]</sup>

### 2.3. The Role of Hole Enrichment toward Reversible NO<sub>2</sub> Sensing

Key to synergistically deploying both conductors in our hybrid films is the electronic characteristic at the heterojunctions formed between cP and cMOFs, as well as the distribution of such heterojunctions throughout the bulk. Particularly, the activation energy for charge carrier transport in response to NO<sub>2</sub> adsorption is pivotal for enhancing the sensing performance of hybrid films. Here we sought to evaluate the sensor reversibility at room temperature by monitoring the channel resistance recovery before and after NO<sub>2</sub> exposure. As discussed above and confirmed by solid state characterizations, the structural configuration of the hybrid film (i.e., lowered film crystallinity and uni-

form distribution of cMOF crystallites within the cP bulk) accounts for enhancement in sensitivity and its retention. Given that our cP@cMOFs-based sensors also exhibit excellent signal recovery, we sought to mechanistically understand the impact of these features on the adsorption and desorption kinetics of NO<sub>2</sub> gas. In MOF-based NO<sub>2</sub> sensors, reducing the sensor response times, and more importantly, increasing the desorption rate constant ( $k_{des}$ ) to achieve reversible sensing have been challenging.<sup>[26]</sup>

Without relying on external stimuli or addition of inactive components, the newly designed cP@cMOFs hybridization provides a thermodynamic solution to irreversible detection of NO<sub>2</sub>. The experimentally constructed energy band diagrams showing respective HOMO levels with respect to fermi level reveal p-type cP as the most hole-rich component (Figure 3a; Figures S19, S20 and Table S1, Supporting Information). In all studied cMOF cases, the two materials are energetically close enough allowing us to hypothesize that, upon hybridization, beyond the formation of microscopic interfaces throughout the bulk, the cP-cMOF heterojunctions establish an electronic equilibrium, and the majority of carriers occupy a shared Fermi level (Figure 3a). In other words, a hole transfer from the cP to the cMOF is thermodynamically favorable forming a hybrid and hole-enriched cMOF state (Figure 3a; Figures S20 and S21, Supporting Information).<sup>[50,51]</sup> This injection of holes into the cMOF's electronic configuration alters the interaction between NO<sub>2</sub> and the sensing channel by lowering the binding energy (the primary source of irreversible sensing, Figure S22, Supporting Information), resulting in reversible sensing behavior, even at room temperature (Figure 3a). Prior to this work, the desorption of NO<sub>2</sub> gas from MOF sorbate materials has been achieved using elevated temperatures, high energy radiation, or the incorporation of heavy metals in the active layer.<sup>[26]</sup> The hybridization strategy we report here is much more straightforward and holds the potential for generalization onto essentially any conductive MOF structure.

To test our proposed working mechanism, we first examined the XPS spectra of the active material before and after NO<sub>2</sub> exposure. The oxidative effect of NO<sub>2</sub> on the sensing materials was evidenced by subsequent charge redistribution around the metal nodes to compensate for the charge imbalance. High-resolution XPS spectra of the characteristic metal peaks (e.g., Cu 2p) reveal a significant change in the ratio between oxidation states of the metal (e.g., Cu<sup>1+</sup> and Cu<sup>2+</sup>). In the case of Cu<sub>3</sub>(HHTP)<sub>2</sub> films, substantial change in the oxidation state of the Cu was evidenced by a decrease in the Cu<sup>1+</sup> (≈933 eV)/Cu<sup>2+</sup> (≈935 eV) ratio from 1.17 to 1.09 after exposure to NO<sub>2</sub> (Figure 3b). Concomitantly, in the pristine MOF samples, despite the high vacuum conditions during XPS measurements, the adsorption and binding of NO<sub>2</sub> molecules were evidenced by a signature peak at 403.9 eV (Figure 3c). In contrast, the hybrid films exhibit no discernable signal from this N 1s peak within the same desorption timescale (Figure 3d), indicative of nearly complete desorption of NO<sub>2</sub> gas from the hybrid films. We associate this complete desorption with the formation of a new Fermi level upon hole enrichment, thus weakening the binding between the gas molecules and the cMOF sites. This labile binding between NO<sub>2</sub> molecules and our cP@cMOFs films would thus be the key

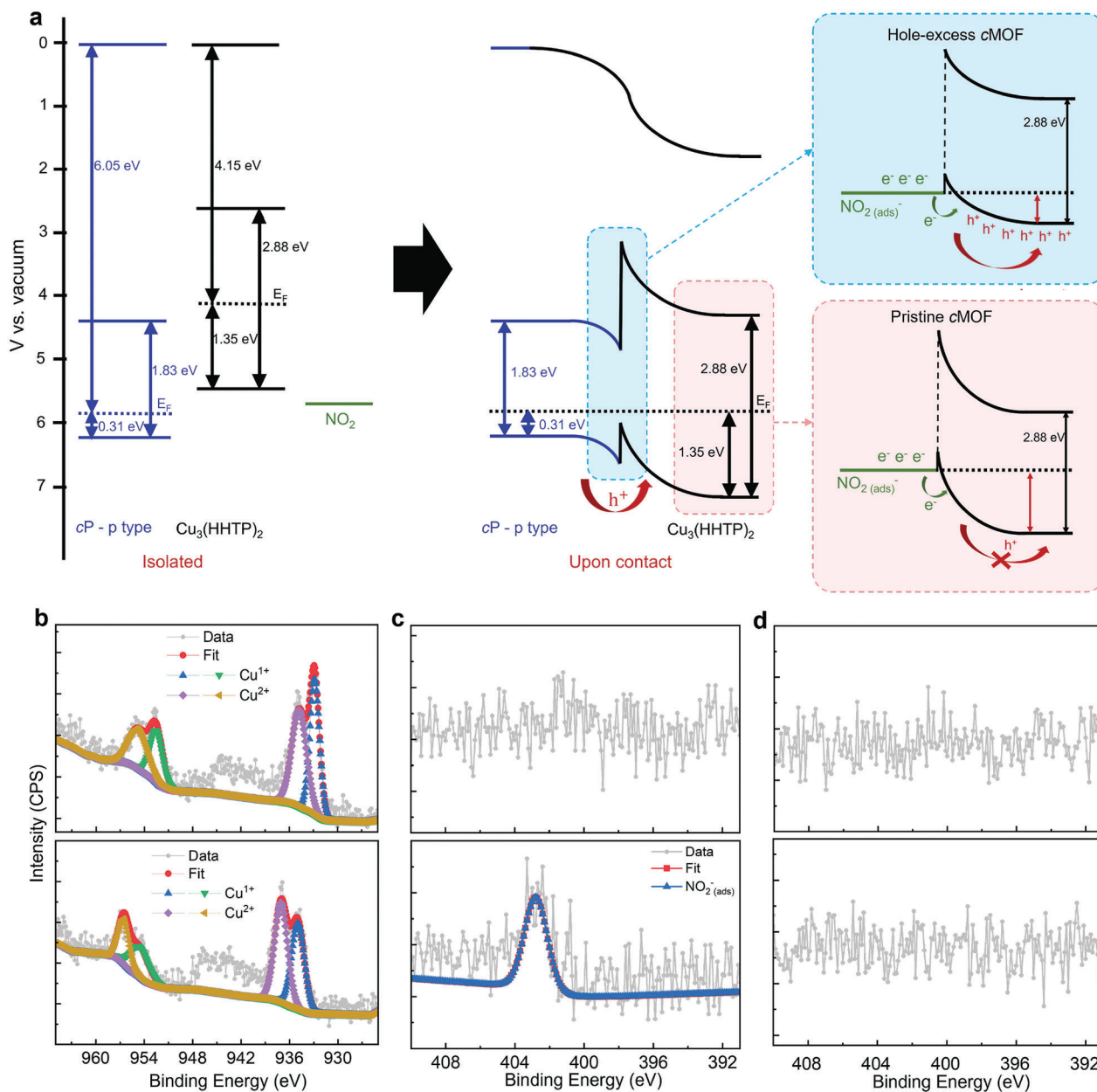


**Figure 3.** Hole enrichment in *c*MOFs and its impact on analyte binding. a) Experimentally constructed energy level diagram of *c*P and representative *c*MOF (full data for all *c*MOFs studied can be found in Figures S19 and S20, Supporting Information) and proposed mechanism/rationale for enhanced recovery upon hybrid. b) High resolution XPS spectra of Cu 2p peak region of Cu<sub>3</sub>(HHTP)<sub>2</sub>, before (top) and after (bottom) NO<sub>2</sub> exposure. c, d) High resolution XPS spectra of N 1s peak region of c) Cu<sub>3</sub>(HHTP)<sub>2</sub> and d) *c*P@Cu<sub>3</sub>(HHTP)<sub>2</sub>, respectively, before (top) and after (bottom) NO<sub>2</sub> exposure.

rationale to the observed dynamic response in the chemiresistive sensors.

We further corroborated this sensing mechanism by experimentally monitoring the sensor's recovery kinetics upon hybridization. We employed a mass action law of gas adsorption reactions on both *c*MOFs and *c*P@*c*MOFs and computed the response and recovery kinetics for NO<sub>2</sub> sensing. Our calculations assumed that the quantity of gas adsorbed on the surface is directly related to the sensors' response. We then calculated respective rate constants according to previous works (i.e.,  $k_{\text{ads}}$  for gas adsorption and  $k_{\text{des}}$  for the desorption)<sup>[52,53]</sup> by fitting the

sensor's response graphs using Equations (2) and (3) below for six distinct *c*MOFs and corresponding *c*P@*c*MOFs (Figure S23, Supporting Information).

$$R(t) \text{ for NO}_2 \text{ adsorption} = R_{\text{max}} \times \frac{C_a K}{1 + C_a K} \left( 1 - \exp \left[ -\frac{1 + C_g K}{K} \times k_{\text{ads}} t \right] \right) \quad (2)$$

$$R(t) \text{ for NO}_2 \text{ desorption} = R_0 \exp [-k_{\text{des}} t] \quad (3)$$

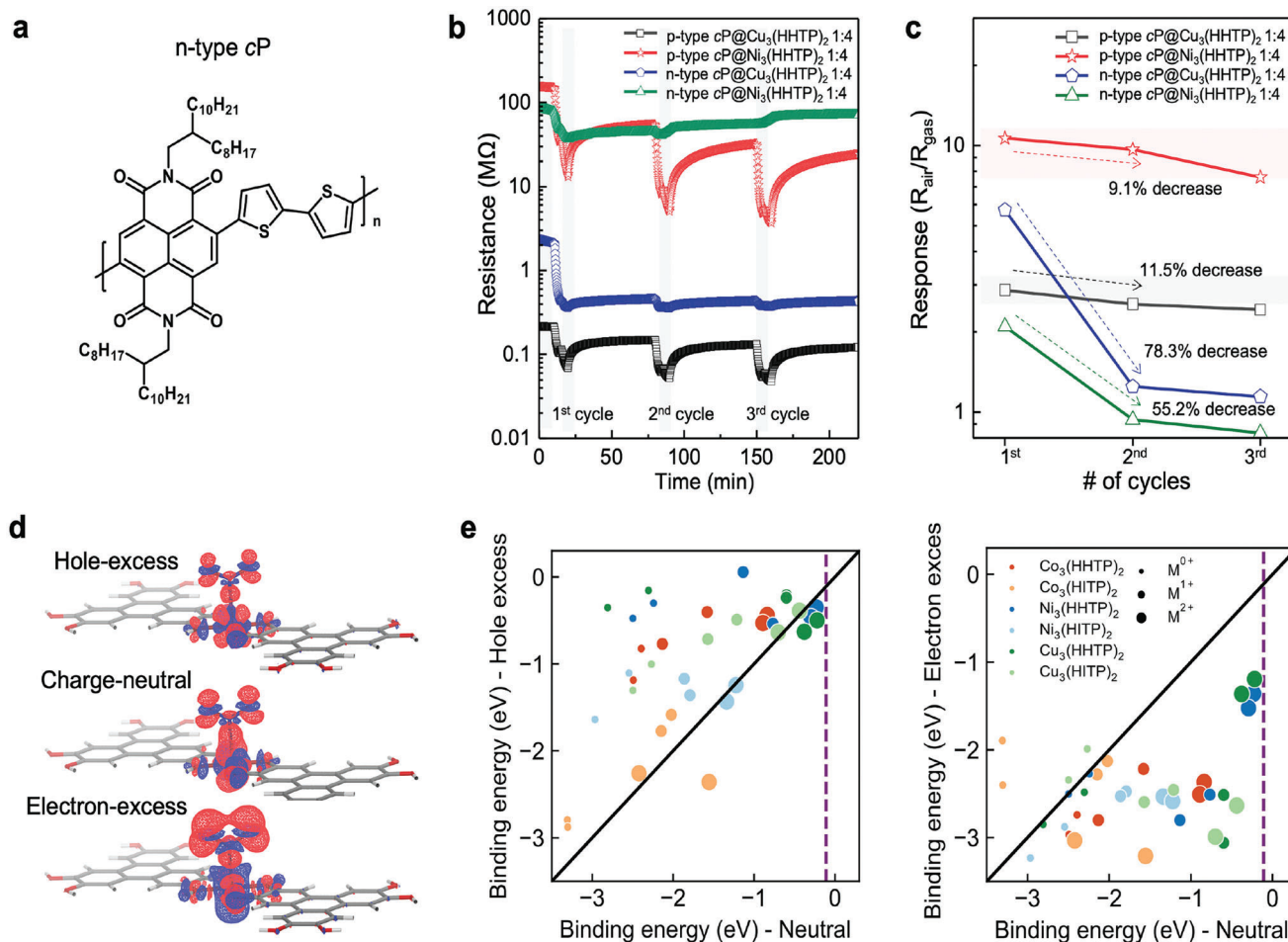


**Figure 4.** Relationship between binding energy and sensor performance. a) Chemical structure of n-type polymer studied. b) Dynamic resistance transitions with varied types of polymers in hybrid. c) Response profile with varied types of polymers in hybrid. d) Differences in charge density before and after NO<sub>2</sub> binding to the cMOF cluster for three system conditions: hole-excess, charge-neutral, and electron-excess, calculated as  $\rho(\text{Cluster} + \text{NO}_2) - \rho(\text{Cluster}) - \rho(\text{NO}_2)$ , where  $\rho$  is the charge density. The red surface denotes an increase in charge density upon NO<sub>2</sub> binding, while the blue surface denotes a decrease. An iso-surface value of  $0.0025 \text{ e}^{-1} \text{ \AA}^{-3}$  has been applied. e) Binding energy of cMOF and NO<sub>2</sub> when the cMOF has an excess hole (left) and an excess electron (right), compared to charge-neutral cMOF. Both adsorption cases, where NO<sub>2</sub> binds either through the O or N atom, are illustrated. The purple dashed line represents the average binding energy between the cP and NO<sub>2</sub>. The black solid line indicates parity.

Here,  $R_0$  is the baseline response in air,  $R_{\text{max}}$  is the maximum response,  $C_a$  is the gas concentration,  $t$  is time, and  $K$  is an equilibrium constant ( $k_{\text{ads}}/k_{\text{des}}$ ).<sup>[52]</sup> In all cases, cP@cMOFs displayed remarkably improved desorption kinetics compared to their corresponding pristine cMOFs counterparts. Notably, the  $k_{\text{des}}$  for cP@Cu<sub>3</sub>(HITP)<sub>2</sub> was measured to be 93.7-fold higher compared to that of pristine Cu<sub>3</sub>(HITP)<sub>2</sub>. Interestingly, the  $k_{\text{ads}}$  values for all cP@cMOFs exhibited minimal changes when compared to those of pristine cMOFs. It was thus evident that the dominant factor for enhancing reversibility in the composite systems is the thermodynamic effect from the hole enrichment, rather than structural factors. Note that for Cu<sub>3</sub>(HITP)<sub>2</sub> and Ni<sub>3</sub>(HHTP)<sub>2</sub>, which showed n-type resistive variation upon NO<sub>2</sub> exposure (oxidizing gas), a higher amount of cP was required than other cMOFs to achieve the optimal ratio for reversibility (Figures S10–S12, S14, Supporting Information). Serendipitously, these two systems also exhibit significantly larger ( $E_F - E_V$ ) values relative to the cP in energy level diagram, making the

hole enrichment more energy consuming. With the same rationale, superior room temperature reversibility was observed in pristine Co-based cMOFs compared to other pristine cMOFs and could be attributed to their notably lower ( $E_F - E_V$ ) value ( $\approx 0.5 \text{ eV}$ ) (thus inherent abundance of hole carrier density), set aside lower crystallinity (Figure S24, Supporting Information).

To verify the role of hole enrichment and test potential countereffect from electron enrichment, we substituted the cP component in our hybrid films with an n-type polymer (in this case, poly[[N,N'-bis(2-octyldodecyl)-naphthalene-1,4,5,8-bis(dicarboximide)-2,6-diyl]-alt-5,5'-(2,2'-bithiophene)]), also known as N2200) (Figure 4a). We then fabricated four types of sensors, that is, p-type cP@Cu<sub>3</sub>(HHTP)<sub>2</sub>, p-type cP@Ni<sub>3</sub>(HHTP)<sub>2</sub>, n-type cP@Cu<sub>3</sub>(HHTP)<sub>2</sub>, and n-type cP@Ni<sub>3</sub>(HHTP)<sub>2</sub>, and compared their sensing behavior under similar conditions. More specifically, we monitored the channel resistance recovery after 3 cyclic exposures of the sensor to 2.5 ppm NO<sub>2</sub>. P-type cP-based composites exhibited reversible

sensing behaviors with minimal reduction in response, 9.1% and 11.5%, respectively, after the first cycle NO<sub>2</sub> exposure (Figure 4b,c). Conversely, n-type cP-based composites demonstrated a dramatically diminished response after the first cycle. Furthermore, exposure to higher NO<sub>2</sub> concentrations in subsequent cycles showed no further change in the channel resistance for n-type composites (Figure S25, Supporting Information) indicative of a dosimetric sensing behavior. For instance, n-type cP@Cu<sub>3</sub>(HHTP)<sub>2</sub> exhibited a higher response during the initial cycle, attributed to its abundant electron concentration facilitating electron donation to NO<sub>2</sub>, but this enhanced response rapidly diminished by 78.3% during the second cycle, attributable to the incomplete recovery (or irreversible kinetics) (Figure 4c). These results effectively emphasize the significance of hole enrichment in the hybrid films enabled by the polymeric component and its effect on the desorption of NO<sub>2</sub> gas, promoting favorable recovery kinetics.

Using density functional theory (DFT) calculations, we also calculated the binding energies between the gas molecules and the sensing material to gain further insight into the effect of cP hybridization on the observed sensing behaviors.<sup>[54,55]</sup> For our simulations, instead of modeling the entire cP@cMOFs systems, we represented cP@cMOFs with p/n-type cP as pure cMOFs with an additional injected hole/electron. By comparing the hybrid systems with the pure, charge-neutral cMOFs, this approach allows us to focus on the hole/electron enrichment effect of cPs on cMOFs. For all six cMOFs under consideration, our simulations considered three possible metal oxidation states, +0, +1, and +2 on the metal node (Figure 4d and Figure S26, Supporting Information). Across all cMOFs, we observed that hole-enriched states exhibit lower binding energy than their neutral state and electron-rich states (Figure 4e). These simulation results thus further supported our rationale of hole-enrichment as a major contributor to NO<sub>2</sub> desorption and thus sensing reversibility. Note that the case of Co-based cMOFs discussed above also shows binding energies on par with other cMOFs, thus underscoring the importance of other contributing factors to the sensing kinetics such as film crystallinity and crystallite size (Figure S24c,d, Supporting Information). We could thus conclude that, in hole-excess scenarios, less electronic charge is transferred from the metal nodes to NO<sub>2</sub>, thereby weakening their binding, compared to electron-excess systems (Figure 4b). This charge transfer between the NO<sub>2</sub> and the metal nodes also supports superior selectivity over other gases, such as H<sub>2</sub>S and NH<sub>3</sub>, as evidenced by calculated selectivity data in Figures S22 and S27, Supporting Information.

### 3. Conclusions

In conclusion, we propose a hybridization method combining two complementary classes of mixed ionic-electronic conductors (MIECs), conductive polymers, and MOFs (cP and cMOFs). Our approach produces chemiresistors with better cycling stability and sustained dynamic range than those made solely from cMOFs or cPs. We conducted a detailed analysis to understand how hybridization with the cPs enhances the reversibility of cMOFs-based sensors, focusing on energy band alignments at the material interfaces and their impact on sensing thermodynamics and binding kinetics. Theoretical calculations further eluci-

dated the effect of such hybridization on the interaction between cMOFs and the gaseous analyte. Our approach proves to be versatile toward designing cP/MOF composites with improved performance and processability. The hybridization thus paves the way for more tailored composite-based electronics leveraging the intrinsic properties of both polymers and MOFs.

### 4. Experimental Section

**Materials:** Co(OAc)<sub>2</sub>·4H<sub>2</sub>O (Alfa Aesar), Co(NO<sub>3</sub>)<sub>2</sub>·6H<sub>2</sub>O (Alfa Aesar), Cu(OAc)<sub>2</sub>·xH<sub>2</sub>O (Alfa Aesar), CuSO<sub>4</sub>·5H<sub>2</sub>O (Alfa Aesar), Ni(OAc)<sub>2</sub>·4H<sub>2</sub>O (Strem), and NaOAc (Alfa Aesar) were used without further purification. 2,3,6,7,10,11-hexaaminotriphenylene hexahydrochloride (HATP-6HCl) was prepared according to a procedure published elsewhere.<sup>[56]</sup> HHTP hydrate (C<sub>18</sub>H<sub>12</sub>O<sub>6</sub>·H<sub>2</sub>O, 95%) was purchased from Tokyo Chemical Industry. For the synthesis of HHTP with higher crystallinity, recrystallization of HHTP ligand was conducted. *N,N*-dimethylformamide, acetone, and methanol were used as received without further purification. Further synthetic details can be found in the Supporting Information.

**cP@cMOF Hybrid Film Processing:** A polymer solution of 10 mg mL<sup>-1</sup> in chloroform was prepared and stirred for 30 min at 35 °C. The cMOFs were initially dispersed in deionized water and ethanol, for M<sub>3</sub>(HITP)<sub>2</sub> series and M<sub>3</sub>(HHTP)<sub>2</sub> series, respectively, immediately after synthesis and filtration. Subsequently, the dispersed cMOFs were sonicated for 5–30 min and blended with the polymer solution in an appropriate w/w ratio to create the final solution for the hybrid film.

**PXRD:** PXRD analysis was conducted using a Bruker Advance II diffractometer equipped with a  $\theta/2\theta$  reflection geometry and Ni-filtered Cu K $\alpha$  radiation ( $K_{\alpha 1} = 1.5406 \text{ \AA}$ ,  $K_{\alpha 2} = 1.5444 \text{ \AA}$ ,  $K_{\alpha 2}/K_{\alpha 1} = 0.5$ ). The tube voltage and current were set as 40 kV and 40 mA, respectively, during operation. Samples were prepared by placing the material on a zero-background silicon crystal plate.

**Spectroscopy Measurements:** XPS measurements were performed using a Physical Electronics PHI Versaprobe II X-ray photoelectron spectrometer equipped with an Al anode as a source. To prepare the samples for analysis, powders were compressed onto copper tapes to ensure complete coverage. The calibration of charge shift was performed by aligning the C1s peak of surface-adsorbed adventitious carbon to 284.8 eV. Ultraviolet-visible (UV-vis) absorption spectra were acquired using a Perkin Elmer 1050 UV-visible-NIR spectrophotometer. Raman spectra were collected on a Raman Reflex instrument utilizing a 532 nm laser source.

**Chemiresistor Fabrication and Characterization:** Gas sensing characterizations involved the coating of sensing materials onto prepatterned Al<sub>2</sub>O<sub>3</sub>-based sensor substrates. These substrates featured two parallel electrodes, each measuring 90  $\mu\text{m}$  in width and spaced 160  $\mu\text{m}$  apart. Following the preparation of the sensing material solutions at a concentration of 10 mg mL<sup>-1</sup>, 5  $\mu\text{L}$  of the solution was cast onto the sensor substrate and dried. Measurement of the resistance of the sensing materials on the electrodes was carried out using a data acquisition system (Agilent 34972A) equipped with a 16-channel multiplexer (Agilent 34902A). For the evaluation of sensing characteristics, the measured resistance values were converted into response values ( $R_{\text{air}}/R_{\text{gas}}$  or  $R_{\text{gas}}/R_{\text{air}}$ ), where  $R_{\text{air}}$  and  $R_{\text{gas}}$  denoted the resistance in air and gas, respectively. For stabilization of the baseline resistance, a baseline air was employed to stabilize the sensors for at least 2 h. To establish concentration-dependent measurements, gas cylinders containing 50 ppm NO<sub>2</sub>, 50 ppm H<sub>2</sub>S, were purchased from Airgas. These gases were then diluted with air using mass flow controllers. Other organic analytes including ethanol, methanol, acetone, toluene, and xylene, were supplied to the sensing chamber using a FlexStream FlexBase module. Further details regarding sensor fabrication steps and sensor dimensions are provided in Supporting Information.

**Experimental Energy Level Measurement:** The electronic band structures were constructed collectively by following measurements: XPS with monochromatic Al K $\alpha = 1486.6 \text{ eV}$  with  $-10 \text{ V}$  bias was conducted



to obtain both cut-off and fermi spectra. A gentle ion gun treatment (Monatomic source gun with 2000 eV, 30 s etch time) was performed to clean the surface. Tauc plots were converted from UV-vis spectra.

**Theoretical Calculation Details: DFT Calculations:** To enable facile control of the charge and oxidation state in the DFT studies, a finite cluster model of the cMOF system was studied using the hybrid B3LYP functional and the composite LACVP\* basis set. These cluster models were extracted from DFT-optimized structures of the full periodic cMOFs with PBE-D2 and a plane wave basis set (kinetic energy cutoff of 400 eV). Full computational details are provided in the Supporting Information.

## Supporting Information

Supporting Information is available from the Wiley Online Library or from the author.

## Acknowledgements

H.R. and D.-H.K. contributed equally to this work. H.R. and A.G. acknowledge financial support from the MIT Climate & Sustainability Consortium (MCSC) as well as the Abdul Latif Jameel Water & Food Systems (JWAFS) Lab at the Massachusetts Institute of Technology (MIT). D.-H.K. and M.D. acknowledge support from the U.S. Department of Energy (DE-SC0023288). Y.C. and H.J.K. acknowledge support for the U.S. Department of Energy (DE-NA0003965).

## Conflict of Interest

The authors declare no conflict of interest.

## Data Availability Statement

The data that support the findings of this study are available in the supplementary material of this article.

## Keywords

chemiresistors, composites, conjugated polymers, metal-organic frameworks

Received: November 19, 2023

Revised: February 20, 2024

Published online:

- [1] H. Furukawa, K. E. Cordova, M. O'Keeffe, O. M. Yaghi, *Science* **2013**, *341*, 1230444.
- [2] D. Sheberla, J. C. Bachman, J. S. Elias, C. J. Sun, Y. Shao-Horn, M. Dincă, *Nat. Mater.* **2017**, *16*, 220.
- [3] S. Bi, H. Banda, M. Chen, L. Niu, M. Chen, T. Wu, J. Wang, R. Wang, J. Feng, T. Chen, M. Dincă, A. A. Kornyshev, G. Feng, *Nat. Mater.* **2020**, *19*, 552.
- [4] A. J. Rieth, A. M. Wright, M. Dincă, *Nat. Rev. Mater.* **2019**, *4*, 708.
- [5] W.-T. Koo, J.-S. Jang, I.-D. Kim, *Chem* **2019**, *5*, 938.
- [6] X. Chen, R. Behboodian, D. Bagnall, M. Taheri, N. Nasiri, *Chemosensors* **2021**, *9*, 316.
- [7] L. E. Kreno, K. Leong, O. K. Farha, M. Allendorf, R. P. Van Duyne, J. T. Hupp, *Chem. Rev.* **2012**, *112*, 1105.
- [8] B. Lal, K. B. Idrees, H. Xie, C. S. Smoljan, S. Shafaie, T. Islamoglu, O. K. Farha, *Angew. Chem., Int. Ed.* **2023**, *62*, 202219053.
- [9] Y. K. Jo, S. Y. Jeong, Y. K. Moon, Y. M. Jo, J. W. Yoon, J. H. Lee, *Nat. Commun.* **2021**, *12*, 4955.
- [10] M. Eddaoudi, J. Kim, N. Rosi, D. Vodak, J. Wachter, M. O'Keeffe, O. M. Yaghi, *Science* **2002**, *295*, 69.
- [11] M. G. Campbell, S. F. Liu, T. M. Swager, M. Dincă, *J. Am. Chem. Soc.* **2015**, *137*, 13780.
- [12] M. G. Campbell, D. Sheberla, S. F. Liu, T. M. Swager, M. Dincă, *Angew. Chem., Int. Ed.* **2015**, *54*, 4349.
- [13] H. Thakkar, S. Eastman, Q. Al-Naddaf, A. A. Rownaghi, F. Rezaei, *ACS Appl. Mater. Interfaces* **2017**, *9*, 35908.
- [14] R. Zhang, S. Ji, N. Wang, L. Wang, G. Zhang, J. R. Li, *Angew. Chem., Int. Ed.* **2014**, *53*, 9775.
- [15] Y. Lei, Y. Sun, H. Zhang, L. Liao, S. T. Lee, W. Y. Wong, *Chem. Commun.* **2016**, *52*, 12318.
- [16] L. G. S. Albano, D. H. S. de Camargo, G. R. Schleder, S. G. Deeke, T. P. Vello, L. D. Palermo, C. C. Corrêa, A. Fazzio, C. Wöll, C. C. B. Bufon, *Small* **2021**, *17*, 2101475.
- [17] R. M. L. da Silva, L. G. S. Albano, T. P. Vello, W. W. R. de Araújo, D. H. S. de Camargo, L. D. Palermo, C. C. Corrêa, C. Wöll, C. C. B. Bufon, *Adv. Electron. Mater.* **2022**, *8*, 2200175.
- [18] Y. Liu, Y. Wei, M. Liu, Y. Bai, X. Wang, S. Shang, C. Du, W. Gao, J. Chen, Y. Liu, *Adv. Mater.* **2021**, *33*, 2007741.
- [19] C. Park, W. T. Koo, S. Chong, H. Shin, Y. H. Kim, H. J. Cho, J. S. Jang, D. H. Kim, J. Lee, S. Park, J. Ko, J. Kim, I. D. Kim, *Adv. Mater.* **2021**, *33*, 2101216.
- [20] C. K. Liu, V. Piradi, J. Song, Z. Wang, L. W. Wong, E. H. L. Tan, J. Zhao, X. Zhu, F. Yan, *Adv. Mater.* **2022**, *34*, 2204140.
- [21] Y. M. Jo, K. Lim, J. W. Yoon, Y. K. Jo, Y. K. Moon, H. W. Jang, J. H. Lee, *ACS Cent. Sci.* **2021**, *7*, 1176.
- [22] W. T. Koo, S. J. Kim, J. S. Jang, D. H. Kim, I. D. Kim, *Adv. Sci.* **2019**, *6*, 1900250.
- [23] M.-S. Yao, X.-J. Lv, Z.-H. Fu, W.-H. Li, W.-H. Deng, G.-D. Wu, G. Xu, *Angew. Chem., Int. Ed.* **2017**, *56*, 16510.
- [24] Y.-M. Jo, Y. K. Jo, J.-H. Lee, H. W. Jang, I.-S. Hwang, D. J. Yoo, *Adv. Mater.* **2023**, *35*, 2206842.
- [25] Y. Lin, W.-H. Li, Y. Wen, G.-E. Wang, X.-L. Ye, G. Xu, *Angew. Chem., Int. Ed.* **2021**, *60*, 25758.
- [26] J.-O. Kim, W.-T. Koo, H. Kim, C. Park, T. Lee, C. A. Hutomo, S. Q. Choi, D. S. Kim, I.-D. Kim, S. Park, *Nat. Commun.* **2021**, *12*, 4294.
- [27] A. M. Wright, C. Sun, M. Dincă, *J. Am. Chem. Soc.* **2021**, *143*, 681.
- [28] A. J. Timmons, M. D. Symes, *Chem. Soc. Rev.* **2015**, *44*, 6708.
- [29] H. Z. Li, Y. Pan, Q. Li, Q. Lin, D. Lin, F. Wang, G. Xu, J. Zhang, *J. Mater. Chem. A* **2022**, *11*, 965.
- [30] M. G. Campbell, S. F. Liu, T. M. Swager, M. Dincă, *J. Am. Chem. Soc.* **2015**, *137*, 13780.
- [31] C. M. Amb, A. L. Dyer, J. R. Reynolds, C. M. Amb, A. L. Dyer, J. R. Reynolds, *Chem. Mater.* **2011**, *23*, 397.
- [32] C. M. Amb, P. M. Beaujuge, J. R. Reynolds, *Adv. Mater.* **2010**, *22*, 724.
- [33] H. Roh, S. Yue, H. Hu, K. Chen, H. J. Kulik, A. Gumyusenge, *Adv. Funct. Mater.* **2023**, *33*, 2304893.
- [34] H. Chae, J. M. Han, Y. Ahn, J. E. Kwon, W. H. Lee, B.-G. Kim, *Adv. Mater. Technol.* **2021**, *6*, 2100580.
- [35] Y. Kang, D. H. Kwak, J. E. Kwon, B.-G. Kim, W. H. Lee, *ACS Appl. Mater. Interfaces* **2021**, *13*, 31910.
- [36] S. T. Navale, A. T. Mane, G. D. Khuspe, M. A. Chougule, V. B. Patil, *Synth. Met.* **2014**, *195*, 2159.
- [37] G. G. Yang, D.-H. Kim, S. Samal, J. Choi, H. Roh, C. E. Cunin, H. M. Lee, S. O. Kim, M. Dincă, A. Gumyusenge, *ACS Sens.* **2023**, *8*, 3687.
- [38] R. M. Stolz, A. Mahdavi-Shakib, B. G. Frederick, K. A. Mirica, *Chem. Mater.* **2020**, *32*, 7639.

- [39] S. T. Navale, A. T. Mane, M. A. Chougule, R. D. Sakhare, S. R. Nalage, V. B. Patil, *Synth. Met.* **2014**, 189, 94.
- [40] S. T. Navale, A. T. Mane, G. D. Khuspe, M. A. Chougule, V. B. Patil, *Synth. Met.* **2014**, 195, 228.
- [41] X. B. Yan, Z. J. Han, Y. Yang, B. K. Tay, *Sens. Actuators, B* **2007**, 123, 107.
- [42] R. K. Sonker, B. C. Yadav, G. I. Dzhardimalieva, *J. Inorg. Organomet. Polym. Mater.* **2016**, 26, 1428.
- [43] N. Karmakar, R. Fernandes, S. Jain, U. V. Patil, N. G. Shimpi, N. V. Bhat, D. C. Kothari, *Sens. Actuators, B* **2017**, 242, 118.
- [44] Y. Zhang, J. J. Kim, D. Chen, H. L. Tuller, G. C. Rutledge, *Adv. Funct. Mater.* **2014**, 24, 4005.
- [45] Q. Y. Zheng, M. Yang, X. Dong, X. F. Zhang, X. L. Cheng, L. H. Huo, Z. Major, Y. M. Xu, *Rare Met.* **2023**, 42, 536.
- [46] A. T. Mane, S. T. Navale, V. B. Patil, *Org. Electron.* **2015**, 19, 15.
- [47] S. T. Navale, G. D. Khuspe, M. A. Chougule, V. B. Patil, *Ceram. Int.* **2014**, 40, 8013.
- [48] H. Park, D. H. Kim, B. S. Ma, E. Shin, Y. Kim, T. S. Kim, F. S. Kim, I. D. Kim, B. J. Kim, *Adv. Sci.* **2022**, 9, 2200270.
- [49] X. Su, Z. Zhong, X. Yan, T. Zhang, C. Wang, Y. X. Wang, G. Xu, L. Chen, *Angew. Chem., Int. Ed.* **2023**, 62, 202302645.
- [50] G. Grosso, G. P. Parravicini, *Solid State Physics*, 2nd ed., Academic Press, Cambridge, MA **2014**.
- [51] Z. Yin, M. Tordjman, Y. Lee, A. Vardi, R. Kalish, J. A. Del Alamo, *Sci. Adv.* **2018**, 4, eaau0480.
- [52] C. Y. Lee, M. S. Strano, *Langmuir* **2005**, 21, 5192.
- [53] D.-H. Kim, S. Chong, C. Park, J. Ahn, J.-S. Jang, J. Kim, I.-D. Kim, *Adv. Mater.* **2022**, 34, 2105869.
- [54] K. W. Nam, S. S. Park, R. dos Reis, V. P. Dravid, H. Kim, C. A. Mirkin, J. F. Stoddart, *Nat. Commun.* **2019**, 10, 4948.
- [55] M. E. Foster, K. Sohlberg, C. D. Spataru, M. D. Allendorf, *J. Phys.* **2016**, 120, 15001.
- [56] T. Chen, J. H. Dou, L. Yang, C. Sun, N. J. Libretto, G. Skorupskii, J. T. Miller, M. Dinca, *J. Am. Chem. Soc.* **2020**, 142, 12367.